The Astrophysical Journal, 970:62 (17pp), 2024 July 20 https://doi.org/10.3847/1538-4357/ad4f89

Atmospheric Waves Driving Variability and Cloud Modulation on a Planetary-mass Object

Michael K. Plummer[1,2], Ji Wang (王吉)[2], Étienne Artigau[3,4], René Doyon[4,5], and Genaro Suárez[6]
[1] Department of Physics and Meteorology, United States Air Force Academy, 2354 Fairchild Drive, CO 80840, USA; michaelkplummer@gmail.com
[2] Department of Astronomy, The Ohio State University, 140 West 18th Avenue, Columbus, OH 43210, USA
[3] Département de Physique, Université de Montréal, IREX, Montréal, QC H3C 3J7, Canada
[4] Observatoire du Mont-Mégantic, Université de Montréal, Montréal, QC H3C 3J7, Canada
[5] Institut Trottier de recherche sur les exoplanètes, Département de Physique, Université de Montréal, Canada
[6] Department of Astrophysics, American Museum of Natural History, Central Park West at 79th Street, New York, NY 10024, USA
Received 2024 March 7; revised 2024 May 7; accepted 2024 May 8; published 2024 July 17

Abstract

Planetary-mass objects and brown dwarfs at the transition ($T_{\rm eff} \sim 1300$ K) from relatively red L dwarfs to bluer mid-T dwarfs show enhanced spectrophotometric variability. Multiepoch observations support atmospheric planetary-scale (Kelvin or Rossby) waves as the primary source of this variability; however, large spots associated with the precipitation of silicate and metal clouds have also been theorized and suggested by Doppler imaging. We applied both wave and spotted models to fit near-infrared (NIR), multiband ($Y/J/H/K$) photometry of SIMP J013656.5+093347 (hereafter SIMP0136) collected at the Canada–France–Hawaii Telescope using the Wide-field InfraRed Camera. SIMP0136 is a planetary-mass object ($12.7 \pm 1.0\,M_{\rm J}$) at the L/T transition ($T2 \pm 0.5$) known to exhibit light-curve evolution over multiple rotational periods. We measure the maximum peak-to-peak variability of $6.17\% \pm 0.46\%$, $6.45\% \pm 0.33\%$, $6.51\% \pm 0.42\%$, and $4.33\% \pm 0.38\%$ in the Y, J, H, and K bands, respectively, and find evidence that wave models are preferred for all four NIR bands. Furthermore, we determine that the spot size necessary to reproduce the observed variations is larger than the Rossby deformation radius and Rhines scale, which is unphysical. Through the correlation between light curves produced by the waves and associated color variability, we find evidence of planetary-scale, wave-induced cloud modulation and breakup, similar to Jupiter's atmosphere and supported by general circulation models. We also detect a $93\overset{\circ}{.}8 \pm 7\overset{\circ}{.}4$ (12.7σ) phase shift between the $H-K$ and $J-H$ color time series, providing evidence for complex vertical cloud structure in SIMP0136's atmosphere.

Unified Astronomy Thesaurus concepts: Brown dwarfs (185); T dwarfs (1679); Exoplanet atmospheres (487); Extrasolar gaseous giant planets (509); Exoplanet atmospheric variability (2020)

1. Introduction

Brown dwarfs and planetary-mass objects, either isolated or orbiting host stars at wide separations, have complex atmospheric dynamics and chemistry. Due to their similar temperatures, masses, and chemical compositions (Burrows et al. 2001), they serve as analogs to lower-mass or more closely orbiting gas giant exoplanets.

Spectrophotometric variability suggests active atmospheric dynamics in substellar objects. Silicate clouds have been found to form in early L dwarfs and thicken throughout the mid-L spectral class (Suárez & Metchev 2022). Brown dwarfs at effective temperatures ($T_{\rm eff}$) of ~1300 K (Kirkpatrick 2005, and references therein) transition from the mineral-cloud-rich, late-L dwarfs (Tsuji et al. 1996; Burrows et al. 2006) to the relatively cloud-free, mid-T dwarfs (Burrows & Sharp 1999; Tsuji & Nakajima 2003; Knapp et al. 2004; Cushing & Roellig 2006). These L/T transition dwarfs exhibit elevated variability (Radigan et al. 2014; Radigan 2014; Eriksson et al. 2019; Liu et al. 2024). Younger brown dwarfs with lower surface gravity and planetary-mass objects also show higher variability rates than field brown dwarfs (Vos et al. 2022; Liu et al. 2024). Enhanced L/T transition variability has been historically associated with the precipitation and breakup of mineral cloud decks formed during the L class as the brown dwarf cools toward T-class temperatures (e.g., Ackerman & Marley 2001; Burgasser et al. 2002; Reiners & Basri 2008).

Two primary atmospheric dynamical structures are fueling the enhanced variability according to general circulation models (GCMs): planetary-scale waves (e.g., Kelvin and Rossby waves) and vortices (e.g., storms and eddies; Showman & Kaspi 2013; Zhang & Showman 2014; Showman et al. 2019; Tan & Showman 2021a, 2021b; Tan 2022). Polarimetric observations (Millar-Blanchaer et al. 2020) of the nearby L/T transition, brown dwarf binary system Luhman 16AB (Luhman 2013) suggest that their atmospheres may be dominated by planetary banding. Long-term spectrophotometric observations of L/T transition objects have found varying levels of preference for wave models (Apai et al. 2017, 2021; Zhou et al. 2022; Fuda et al. 2024) presumably contained within these banded structures. Specifically, Zhou et al. (2022) fit VHS J125601.92 −125723.9 b (hereafter VHS 1256 b, L7; Gauza et al. 2015), a young planetary-mass object, with both wave and spotted models and found a small preference for a three-wave model over a combination wave/spot model.

However, Doppler imaging has provided tentative evidence for spotlike features in Luhman 16B through a surface map inferred (Crossfield et al. 2014) using maximum entropy principles. Reanalyzing the same data, Luger et al. (2021) identified similar features using the open-source `starry`

framework. These results must be interpreted with caution, as maximum-entropy-based Doppler imaging (see, e.g., Vogt et al. 1987) does not deliver a unique solution but instead derives a map in which goodness of fit is balanced against the complexity of the image. Crossfield et al. (2014) further highlighted that, as their spectra are sensitive to CO, the inferred maps may be affected by chemical abundance inhomogeneities. Notably, Crossfield et al. (2014) concluded that zonal bands would not be detectable based on the data precision; therefore, a comparison of spotted versus wave models was not possible at the time. Using Hubble Space Telescope (HST) spectrophotometry and the `Aeolus` code, Karalidi et al. (2016) identified two pairs of bright and dark features offset by 180° on Luhman 16B, features that could fit either spotted or wave paradigms.

SIMP J013656.5+093347 (hereafter SIMP0136; Artigau et al. 2006) is a young (200 ± 50 Myr; Gagné et al. 2017), L/T transition (T2 ± 0.5), planetary-mass object ($12.7 \pm 1.0\,M_J$; Gagné et al. 2017) demonstrating high variability ($\gtrsim$5%; Artigau et al. 2009; Radigan et al. 2014; Croll et al. 2016; Eriksson et al. 2019). Because SIMP0136 is a rapid rotator with a measured period of 2.414 ± 0.078 hr (Yang et al. 2016) and $v \sin i = 52.8\ ^{+1.0}_{-1.1}$ km s^{-1} (Vos et al. 2017), surface inhomogeneities (e.g., clouds and storms; Reiners & Basri 2008) may explain its history of significant light-curve evolution (see, e.g., Artigau et al. 2009; Apai et al. 2013, 2017; Croll et al. 2016). Yet, near-infrared (NIR) Spitzer Space Telescope observations over eight epochs and 32 rotations showed that SIMP0136's photometry could be best fit by composite sinusoidal functions of wavenumber $k = 1$, 2; moreover, multiple waves of the same wavenumber with phase offsets can create beating wave patterns, explaining the planetary-mass object's light-curve evolution (Apai et al. 2017). HST studies of SIMP0136 have detected wavelength-dependent amplitude and phase shifts as well as pressure-dependent contribution functions (Apai et al. 2013; Yang et al. 2016; McCarthy et al. 2024), hinting at a complex vertical atmospheric structure. Supporting this interpretation, spectroscopic retrievals (Vos et al. 2023) and spectrophotometry (McCarthy et al. 2024) have inferred multiple patchy layers of forsterite and iron clouds in SIMP0136's atmosphere.

In this paper, we analyze multiband ($Y/J/H/K$) photometry collected for SIMP0136 on two consecutive nights to learn about the source of spectrophotometric variability and atmospheric dynamics. We fit the photometry with both waves and spotted models, assess the performance of each model, and perform a model selection based on goodness-of-fit tests. This leads to insight into SIMP0136's horizontal and vertical atmospheric structure.

The paper is structured as follows. In Section 2, we explain our observational strategy and data reduction methods and compare the periodic signals of SIMP0136 and our reference stars. We next detail the wave (Section 3.1) and storm/spotted (Section 3.2) models we use to fit the observed light curves and also explain the metrics we employ to assess model performance (Section 3.3). In Section 4, we compare our model fits for the photometry of two consecutive nights (Sections 4.1 and 4.2). We discuss the implications for our research in terms of a preferred driver of variability (Section 5.1), planetary-scale waves' physical nature (Section 5.2), correlation between waves and cloud modulation (Section 5.3), and a detected phase offset between color series (Section 5.4). We summarize our findings and suggest future work in Section 6.

2. Observations and Data Reduction

NIR photometric observations were conducted at the Canada–France–Hawaii Telescope (CFHT) on the summit of Maunakea, Hawaii, using the Wide-field InfraRed Camera (WIRCam; Puget et al. 2004). On 2012 October 14 (UT), exclusively J-band observations were collected, resulting in high-cadence ($\Delta t = 0.0715$ hr) data. The following night, 2012 October 15 (UT), the filter was alternated between the Y, J, H, and K bands, resulting in multicolor but lower-cadence ($\Delta t = 0.385$ hr) light curves.

We used the frames reduced by CFHT's default pipeline (`iiwi` version 2.1.100; Thanjavur et al. 2011) and extracted the photometry from flat-fielded and sky-subtracted frames ("p" files in the cadc science archive[7]) using a fixed 2.″8 aperture radius. The 50th and 90th percentile seeing values were 1.″18 and 1.″43.

The photometric time series were obtained using 12 subexposures with a per-subexposure effective exposure time of 8 s. The photometry was measured in individual subexposures and averaged to the values used for scientific analysis. As the sequence of subexposures is short (∼4 minutes, including interexposure overheads), we can assume that SIMP0136 and the reference stars are stable in flux within the subexposure sequence. We therefore use the dispersion of the 12 subexposure photometric measurements to determine the photometric uncertainty of their mean value.

The top two panels of Figures 1 and 2 display the raw (but normalized against each star's mean) light curves for SIMP0136 and five reference comparison stars for the 2012 October 14 and 2012 October 15 observations, respectively. To correct for systematic effects, SIMP0136 and the comparison stars were divided by the mean normalized light curves of the comparison stars. The corrected light curves can be seen in the bottom two panels of Figures 1 and 2.

The reference comparison stars (see Table 1) were selected due to their location within the NIR detector's field of view, brightness, and lack of periodicity near SIMP0136's known rotational rate. As an initial test of SIMP0136's and the comparison stars' periodicities, we performed Lomb–Scargle (L-S) periodogram analysis (Lomb 1976; Scargle 1982) using the `LombScargle` Python class within `astropy` (Astropy Collaboration et al. 2013, 2018, 2022). Figure 3 shows the results for the J-band observations on 2012 October 14. SIMP0136 exhibits two peaks above a 1% false-alarm probability (FAP) corresponding to the rotational period (∼2.42 hr) found in previous studies (e.g., Artigau et al. 2009) and half the rotational period (∼1.21 hr). The reference stars do not contain signals above the 1% FAP near SIMP0136's rotational period. In the Appendix, we test the reference stars for trends between air mass and seeing variations and measured brightness. We also confirm the reference stars' nonvariability at periods of <1 day using external data from the Transiting Exoplanet Survey Satellite (TESS; Ricker et al. 2015).

[7] https://www.cadc-ccda.hia-iha.nrc-cnrc.gc.ca/en/search/?collection=CFHT&noexec=true

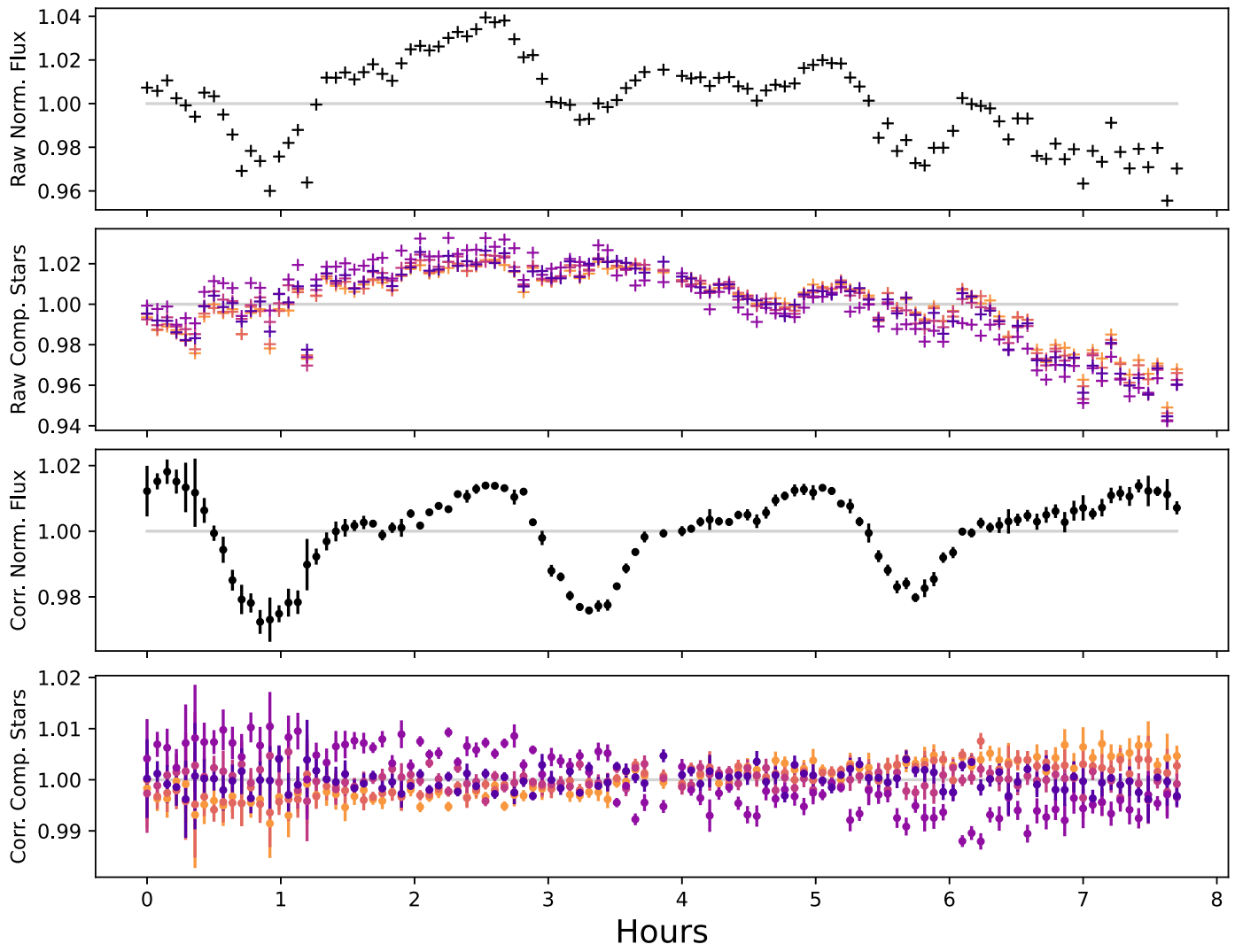

Figure 1. High-cadence *J*-band photometry of SIMP0136 collected at the CFHT on 2012 October 14. (Top) Raw normalized light curves of SIMP0136. (Second row) Raw normalized light curves of comparison stars. (Third row) Corrected light curves for SIMP0136. (Bottom) Corrected light curves for comparison stars. Decreased photometric accuracy can be seen at the beginning and end of the observation period due to increased air mass.

3. Methods

To model both planetary-scale atmospheric waves and storms/spots, we modify `Imber` (Plummer 2023, 2024a), an open-source Python code. The `Imber` code, the data used in this work, and a tutorial for duplicating our results and figures are openly available via GitHub[8] and Zenodo (Plummer 2024b). `Imber` was developed and refined in Plummer & Wang (2022, 2023). A more extensive and complete description of the package and its underlying methodology can be found in those articles.

`Imber` was created to analytically infer surface inhomogeneities (e.g., magnetic spots, storms, and vortices) on stars, brown dwarfs, and directly imaged exoplanets using a Doppler-imaging-based technique for spectroscopic data and light-curve inversion for photometry. It allows both data types to be included for an integrated multimodal solution. `Imber` also includes a numerical simulation module with a full 3D grid to produce forward models of spectra, spectral line profiles, and light curves. Plummer & Wang (2022) demonstrated that the numerical and analytical models produce outputs (e.g., line profiles, light curves) with residuals between the two on the order of 0.001%.

This section details the models we employ as well as the metrics by which we evaluate those models. In Section 3.1, we describe the wave model we use to fit the photometry. Section 3.2 provides a brief description of the spotted model we implement via light-curve inversion. To infer both wave and spot parameters, we employ Bayesian inference, specifically dynamic nested sampling (Skilling 2004, 2006; Higson et al. 2019) via `Dynesty` (Speagle 2020), within our framework. The inferred models are evaluated based on fit controlled for the number of free parameters (see Section 3.3).

3.1. Wave Model

For our wave model, we adopt the same approach as Zhou et al. (2022) based on Apai et al. (2017, 2021) and include a bias (C_0), a linear term (C_1), and the sum of multiple (N)

[8] https://github.com/mkplummer/Imber

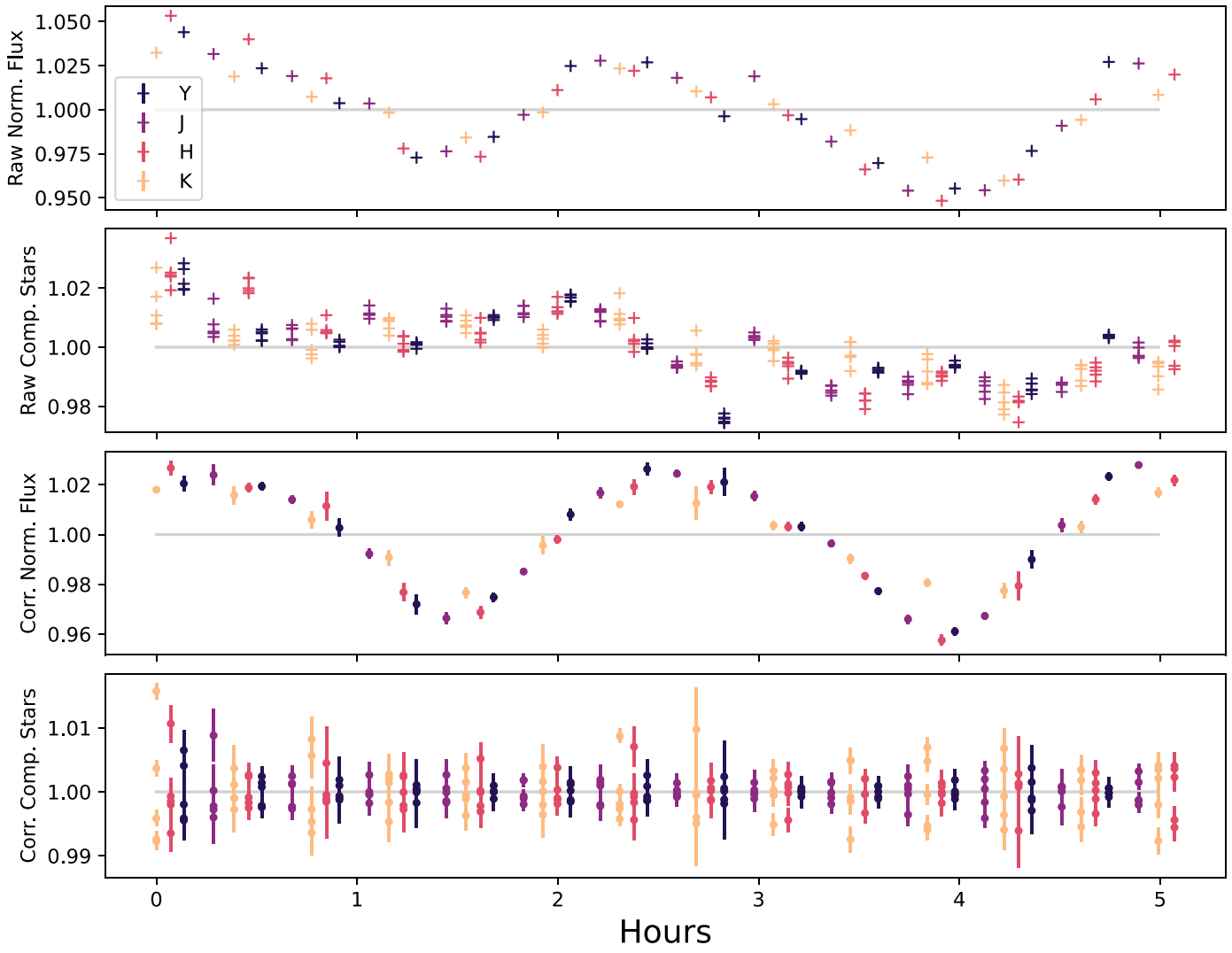

Figure 2. Low-cadence $Y/J/H/K$ photometry of SIMP0136 collected at the CFHT on 2012 October 15. (Top) Raw normalized light curves of SIMP0136. (Second row) Raw normalized light curves of comparison stars. (Third row) Corrected light curves for SIMP0136. (Bottom) Corrected light curves for comparison stars.

Table 1
Reference Comparison Stars (Cutri et al. 2003; Stassun et al. 2018; Gaia Collaboration et al. 2023)

ID	R.A. Gaia DR3	Decl. Gaia DR3	J 2MASS	H 2MASS	K 2MASS	TIC
1	024.27989553291	+09.5853296147900	13.428	12.699	12.54	346896162
2	024.26213598995	+09.62180319580	12.722	12.383	12.355	346896137
3	024.16122843640	+09.55283749631	13.762	13.451	13.366	346894237
4	024.17202937970	+09.57556394562	13.221	12.871	12.828	346894244
5	024.21515175402	+09.60840662161	14.290	13.904	13.727	346894261

sinusoidal functions:

$$F(t) = C_0 + C_1 t + \sum_i^N A_i \sin(2\pi t / P_i + \theta_i). \quad (1)$$

The linear term (C_1) accounts for a variation on timescales greater than our observation window. A_i, P_i, and θ_i are the ith order amplitude, period, and phase. The free parameters are C_0, C_1, A_i, P_i, and θ_i. Each additional wave adds three additional free parameters; therefore, the expression for the number of free parameters is $m = 3N + 2$.

Uniform priors are assumed for each free parameter in the wave model. Based on SIMP0136's photometric variation of $\sim$5% in each NIR band, the individual wave component amplitudes (A_i) have a range of $2.5\% \pm 2.5\%$. For the period, we adjust the range of periods based on the results of the L-S periodogram in Section 2. Phase varies by $180° \pm 180°$. The bias is allowed to vary by ± 0.25 and the slope by $\pm 0.1\ \mathrm{hr}^{-1}$.

3.2. Storm/Spot Model

`Imber` was initially designed to both simulate spotted features' effects on observations and infer spot parameters given

a set of observational data. Here, we will briefly summarize the spotted model, but the authors refer readers to Plummer & Wang (2022, 2023) for a more rigorous explanation.

To enable computationally inexpensive Bayesian inference, the 2D stellar/substellar surface is represented by a 1D flux array. Baseline flux is modeled with a broadening kernel (Gray 2008) with linear limb-darkening coefficients selected based on values derived by fitting Luhman 16B's spectral line profile (due to similar spectral type and $T_{\rm eff}$) in Plummer & Wang (2022). Spots are modeled as Gaussian deviations to the baseline kernel to which bright spots add flux and dark spots subtract flux. The added/subtracted flux is scaled by the spot's temperature contrast and apparent size. Size is determined based on the spot radius and also latitudinal and longitudinal foreshortening due to the viewing angle (Lambert's cosine law). Object inclination is accounted for with rotation matrices (Euler–Rodrigues formula; Shuster 1993). The summed 1D flux at each time step is used to create the modeled light curve.

For this work, `Imber` was modified to allow both radius and temperature contrast to evolve in value from one rotation to the next. The code currently works by setting the rotation by which the evolution is complete; it then varies the spot parameter (radius or contrast) linearly at each time step over one full rotation, thereby accounting for dynamic atmospheric activity.

The number of spots drives the number of free parameters for these models. Each spot has a latitude, longitude, radius, and temperature contrast. Similar to the wave models, we also include a bias to account for an unknown mean baseline flux. If spot evolution is incorporated into the model, each evolution increases the number of spot parameters. The model leads to the following expression for the number of free parameters: $m = 1 + N(4 + 2E)$, where N is the number of spots and E is the number of spot evolutions.

Similar to the wave model, we assume uniform priors for the spotted model free parameters. Latitude and longitude priors encompass the entire sphere ($\pm 90^\circ$ and $\pm 180^\circ$, respectively). Radius is sampled from $30^\circ \pm 30^\circ$. Contrast varies uniformly from $+1$ (completely dark spot) to -1 (twice the background brightness).

3.3. Model Performance Metrics

To compare the relative merits of each model, we will use goodness-of-fit tests (χ^2 and reduced χ^2) and the Bayesian information criterion (BIC) to provide metrics. Reduced χ^2 is computed as

$$\chi^2_\nu = \frac{\chi^2}{\nu} = \frac{\chi^2}{n-m} = \frac{1}{n-m}\sum_{i=1}^{n}\frac{(O_i - M_i)^2}{\sigma^2}, \quad (2)$$

where n is the number of data points (observations); m is the number of free parameters; O_i and M_i are the ith data points for the observation and model, respectively; and σ is the photometric uncertainty.

We use the following expression to calculate BIC (Kass & Raftery 1995):

$$\mathrm{BIC} = \chi^2 + m\ln(n). \quad (3)$$

For χ^2, χ^2_ν, and BIC, a smaller value denotes a better fit. BIC and χ^2_ν account for both fit and the number of free parameters, thereby weighting against more complex models.

4. Results

In this section, we fit the SIMP0136 NIR photometry collected on 2012 October 14 and 2012 October 15 with both wave (see Section 3.1) and spotted models (see Section 3.2) to determine the primary driver of the planetary-mass object's spectrophotometric variability. Table 2 summarizes the computed χ^2_ν, χ^2, and BIC values for each model. The preferred model (ranked by χ^2_ν) is shown at the top of each category; each alternate model has an associated $\Delta\chi^2$ and ΔBIC, denoting its performance with respect to the best-fitting model.

4.1. High-cadence Data

We fit the 2012 October 14 high-cadence J-band data with both wave and spotted models. For the wave models, we test $N = 1$–3 with improvement seen up to and including three waves. We find that the three-wave model is strongly preferred. Four-wave models fail to converge, presumably due to too many free parameters ($m = 14$). We test one- and two-spot models, both with and without spot evolution. We attempt three-spot models, but the models do not converge on a solution.

Figure 4 shows the preferred three-wave model with wavenumbers $k = 1$, 2, and 3. Wave amplitude decreases with increasing wavenumber. The $k = 1$ period ($P_1 = 2.41 \pm 0.01$ hr) matches the previously measured rotational period (2.414 ± 0.078 hr; Yang et al. 2016). The $k = 2$ and $k = 3$ waves' periods ($P_2 = 1.21 \pm 0.01$ hr and $P_3 = 0.80 \pm 0.01$ hr) are approximately half and one-third SIMP0136's rotational period. Based on the Nyquist sampling criterion alone, the 2012 October 14 J-band mean cadence ($\Delta t = 0.0715$ hr) can theoretically detect signals with wavenumbers $\lesssim 16$, but higher-order wave components may be missed due to an insufficient signal-to-noise ratio. The wave component parameters are summarized in Table 3.

We find that SIMP0136 has a J-band peak-to-peak variability of $3.85\% \pm 0.14\%$ for 2012 October 14. Here we compute the percent variability based on the minimum and maximum values of the three-wave model during the observational period. The uncertainty value is computed using the mean of the model standard deviation. The photometric variability measured for 2012 October 14 is lower than that seen the following night, suggesting a dynamic atmosphere over a relatively short time span.

The retrieved three-wave model contains two features that could allow for multirotational light-curve evolution: offset phases between components and a long-term linear term (slope). The offset phases allow the superposition of each wave to create a dynamic observed light curve. The Bayesian inference also retrieves a $+0.03\% \pm 0.01\%\,\mathrm{hr}^{-1}$ linear slope term demonstrating a gradual increase in flux and hints at dynamics on timescales longer than the period of observation.

Here we briefly highlight a few features from less preferred models. The two-wave model (second most preferred) retrieves the same period/wavenumber as the three-wave model's highest-amplitude waves, $k = 1$ and 2, adding further support to the three-wave model. The two-spot model in which spots were allowed to evolve in size and contrast over each rotation returned both a dark spot (radius $\sim 20^\circ$) and a bright spot (radius $\sim 10^\circ$) and was the third most preferred model. The spots were located at opposite polar latitudes ($\sim \pm 60^\circ$) and varied in both size and contrast over each rotation. The spotted model results will be discussed in further detail in Section 5.1.

Table 2
Model Comparison: χ^2, BIC, Observations (n), and Free Parameters (m)

Observation Date	NIR Band	Model	χ^2_ν	χ^2	$\Delta\chi^2$	BIC	ΔBIC	m
2012 Oct 14	J	Three-wave	1.5	149	0	201	0	11
	($n = 109$)	Two-wave	2.4	247	+97.9	284	+ 83.8	8
		Two-spot (evolving)	3.2	302	+154	363	+163	13
		Two-spot	3.9	389	+240	431	+230	9
2012 Oct 15	Y	Two-wave	1.5	7.7	0	29	0	8
	($n = 13$)	One-spot (evolving)	4.4	26.1	+18.4	44.1	+15.9	7
		One-spot	5.7	45.3	+37.6	58.1	+29.9	5
		One-wave	7.3	58.3	+50.6	71.1	+42.9	5
	J	Two-wave	2.1	10.5	0	31.0	0	8
	($n = 13$)	One-spot (evolving)	7.0	41.9	+31.4	59.9	+28.8	7
		One-wave	10.4	82.8	+72.3	95.6	+64.6	5
		One-spot	12.2	97.6	+87.1	110	+79.4	5
	H	Two-wave	1.8	10.5	0	31.6	0	8
	($n = 14$)	One-wave	6.8	61.5	+51.0	74.7	+43.1	5
		One-spot	8.6	77.2	+66.7	90.4	+58.8	5
		One-spot (evolving)	9.1	64.0	+53.5	82.5	+50.9	7
	K	Two-wave	1.0	5.75	0	26.9	0	8
	($n = 14$)	One-wave	2.6	23.5	+17.8	36.7	+9.8	5
		One-spot (evolving)	5.6	39.4	+33.7	57.9	+31.0	7
		One-spot	26.0	234	+228	247	+221	5
	$Y + J + H + K$	Two-wave	11.1	509	0	541	0	8
	($n = 54$)	Two-spot	12.8	576	+67	612	+71.0	9
		One-spot (evolving)	13.7	642	+133	670	+129	7
		One-spot	13.8	675	+166	695	+154	5

Table 3
Inferred Wave Component Parameters: Amplitude (A_i), Period ($_{Pi}$), and Phase Shifts (θ_i)

Observation Date	NIR Band	Wavenumber (k)	A_i (%)	$_{Pi}$ (hr)	θ_i (deg)
2012 Oct 14	J	1	1.29 ± 0.02	2.41 ± 0.01	$112.43^{+2.32}_{-2.33}$
		2	0.81 ± 0.02	1.21 ± 0.01	$17.65^{+3.69}_{-3.84}$
		3	0.21 ± 0.02	0.80 ± 0.01	$239.81^{+16.71}_{-16.83}$
2012 Oct 15	Y	1	2.85 ± 0.11	2.42 ± 0.03	$58.00^{+4.85}_{-5.12}$
		2	0.75 ± 0.11	1.27 ± 0.02	$205.83^{+15.54}_{-15.05}$
	J	1	$2.94^{+0.08}_{-0.07}$	2.43 ± 0.02	$57.95^{+3.14}_{-3.23}$
		2	0.67 ± 0.08	1.26 ± 0.02	$190.91^{+13.78}_{-12.19}$
	H	1	2.86 ± 0.09	2.44 ± 0.03	$56.93^{+4.82}_{-4.94}$
		2	$0.68^{+0.11}_{-0.10}$	1.27 ± 0.02	$182.53^{+15.86}_{-16.58}$
	K	1	1.88 ± 0.09	2.43 ± 0.04	$52.29^{+7.19}_{-7.06}$
		2	0.35 ± 0.10	1.27 ± 0.04	$151.59^{+34.29}_{-32.74}$
	$Y + J + H + K$	1	2.62 ± 0.04	2.41 ± 0.01	$51.95^{+2.11}_{-2.10}$
		2	0.57 ± 0.04	1.26 ± 0.01	$175.41^{+8.44}_{-9.30}$

4.2. Low-cadence Data

The 2012 October 15 observations provide lower-cadence data with significantly fewer data points: 13, 13, 14, and 14 for the Y, J, H, and K bands, respectively. The mean cadence between observations of $\Delta t = 0.385$ hr corresponds to maximum detectable wavenumbers of $\lesssim 3$ based on the Nyquist sampling criterion. For each NIR band, we are only able to constrain $k = 1$ and 2 wave models. Three-wave models do not converge, likely due to the low cadence and small number of observations in each band.

Similar to the high-cadence 2012 October 15 data, multi-wave models outperform spotted models for each individual band and when all four NIR bands are fit simultaneously (see Table 2). The preferred two-wave models for each NIR band are remarkably similar, with each band retrieving $k = 1$, 2 models with periods at the rotational rate and half the rotational rate (see Table 3 and Figure 5). The phase offsets also appear

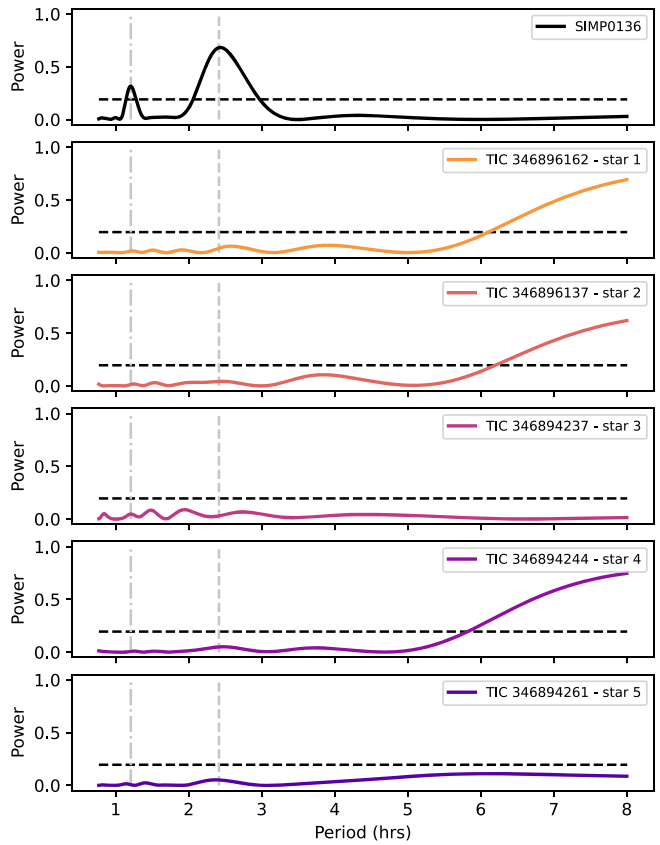

Figure 3. L-S periodogram for *J*-band 2012 October 14 observations. The horizontal dashed black line denotes the 1% FAP. Vertical dashed gray lines denote the SIMP0136 rotational period (∼2.42 hr) and half the rotational period (∼1.21 hr). SIMP0136 shows prominent signals matching these periods. Reference comparison stars do not exhibit significant signals >1% FAP at periodicities near SIMP0136's rotational period.

similar, with each component's $k=1$ wave having a phase between 52° and 58° and $k=2$ phases ranging between 152° and 206° but with overlapping 1σ uncertainties. Matching expectations, the simultaneous, composite $Y+J+H+K$ fit retrieves a two-wave model that is approximately the average of the individual NIR-band solutions.

Using the two-wave models, we compute peak-to-peak variability of $6.17\% \pm 0.46\%$, $6.45\% \pm 0.33\%$, $6.51\% \pm 0.42\%$, and $4.33\% \pm 0.38\%$ for the *Y*, *J*, *H*, and *K* bands, respectively. Both percent variability and uncertainty are computed as described in Section 4.1. The high variability (>5%) found here is broadly consistent with previous observations of SIMP0136 (Artigau et al. 2009; Apai et al. 2013, 2017; Metchev et al. 2013; Radigan et al. 2014; Wilson et al. 2014; Croll et al. 2016; McCarthy et al. 2024).

As can be seen in the bottom panels of Figure 5, each NIR-band retrieval includes a negative linear slope with values of $-0.14\% \pm 0.06\%\,\mathrm{hr}^{-1}$, $-0.16\% \pm 0.04\%\,\mathrm{hr}^{-1}$, $-0.21\% \pm 0.05\%\,\mathrm{hr}^{-1}$, and $-0.16\% \pm 0.05\%\,\mathrm{hr}^{-1}$ for the *Y*, *J*, *H*, and *K* bands, respectively. This is a steeper slope with the opposite sign as that seen in the 2012 October 14 data the night prior. The variation may lend evidence to unmodeled waves or other dynamics with timescales greater than the period of observation.

Spotted models have greater difficulty modeling the low-cadence data. Evolving two-spot models require approximately an equal number of free parameters as there are data points (and are therefore not considered), while nonevolving two-spot models have difficulty converging (with the exception of the composite $Y+J+H+K$ fit, which has the benefit of a higher number of observations). Both evolving and nonevolving one-spot models retrieve polar spots (∼70°–80°) with radii of ∼30°. Evolving one-spot models tend to outperform nonevolving models, with the exception being the *H* band, where spot evolution is preferred by BIC but not χ^2_ν.

5. Discussion

5.1. Storms or Waves as Primary Variability Driver?

As can be seen in Table 2, wave models outperform spotted models in terms of χ^2, χ^2_ν, and BIC. Here we seek to explore physical explanations for these results.

To further understand SIMP0136's atmospheric dynamics, we will use two planetary-scale parameters: the Rossby deformation radius (L_D; e.g., Gill 1982) and the Rhines scale (L_β; Rhines 1975). The Rossby deformation radius is the length at which rotational (Coriolis) effects become important (Gill 1982), and it can also be seen as the typical scale for atmospheric storms and vortices (e.g., Tan & Showman 2021b; Zhou et al. 2022). The Rossby deformation radius is computed (in kilometers) as follows (Showman et al. 2013):

$$L_D = \frac{U}{2\Omega \sin\phi}, \tag{4}$$

where U is the flow speed, Ω is the angular rotational speed, and ϕ is latitude.

At lengths greater than the Rhines scale, atmospheric structures transition from turbulent features to zonal jets as seen on solar system planets (e.g., Cho & Polvani 1996; Showman et al. 2010, 2013; Haqq-Misra et al. 2018); here the Rhines scale is computed (in kilometers),

$$L_\beta = \sqrt{\frac{UR}{2\Omega \cos\phi}}, \tag{5}$$

where R is the object's radius.

Both inferred spots exceed the Rossby deformation radius and Rhines scale for SIMP0136, meaning the retrieved spotted models are likely unphysical. Considering the spotted model with the best χ^2_ν (the high-cadence, *J*-band, two-spot model with size and contrast evolution; see Table 2), we compute the Rossby deformation radius and Rhines scale at the inferred spot latitude. We conservatively assume a flow velocity (U) of $1000\,\mathrm{m\,s}^{-1}$ based on the brown dwarf 2MASS J10475385 +2124234's (Burgasser et al. 1999) measured wind speed of $650\,\mathrm{m\,s}^{-1}$ (Allers et al. 2020). We assume a planetary radius of $1.15\,R_\mathrm{J}$ based on spectral energy distribution analysis of SIMP0136 by Vos et al. (2023). These assumptions result in $L_D = 0.^\circ 9$ and $L_\beta = 11.^\circ 8$ for latitudes of ±60°. The dark spot at latitude $-62.^\circ 36^{+1.37^\circ}_{-1.23^\circ}$ has inferred radii varying from $23.^\circ 68^{+4.67^\circ}_{-3.00^\circ}$ to $20.^\circ 27^{+5.77^\circ}_{-3.31^\circ}$. The bright spot has a latitude of $+56.^\circ 77^{+6.28^\circ}_{-19.04^\circ}$ and radii ranging from $11.^\circ 20^{+3.24^\circ}_{-2.33^\circ}$ to $10.^\circ 78^{+2.73^\circ}_{-1.99^\circ}$. We can see that the dark spot's inferred radius range exceeds L_β, and both spots' radii are far greater than L_D. It is also unlikely that a group of adjacent spots of equivalent summed size are responsible for the observed variability, as the same arguments above would require such spots to be in separate latitudinal bands (based on the Rhines scale) in which

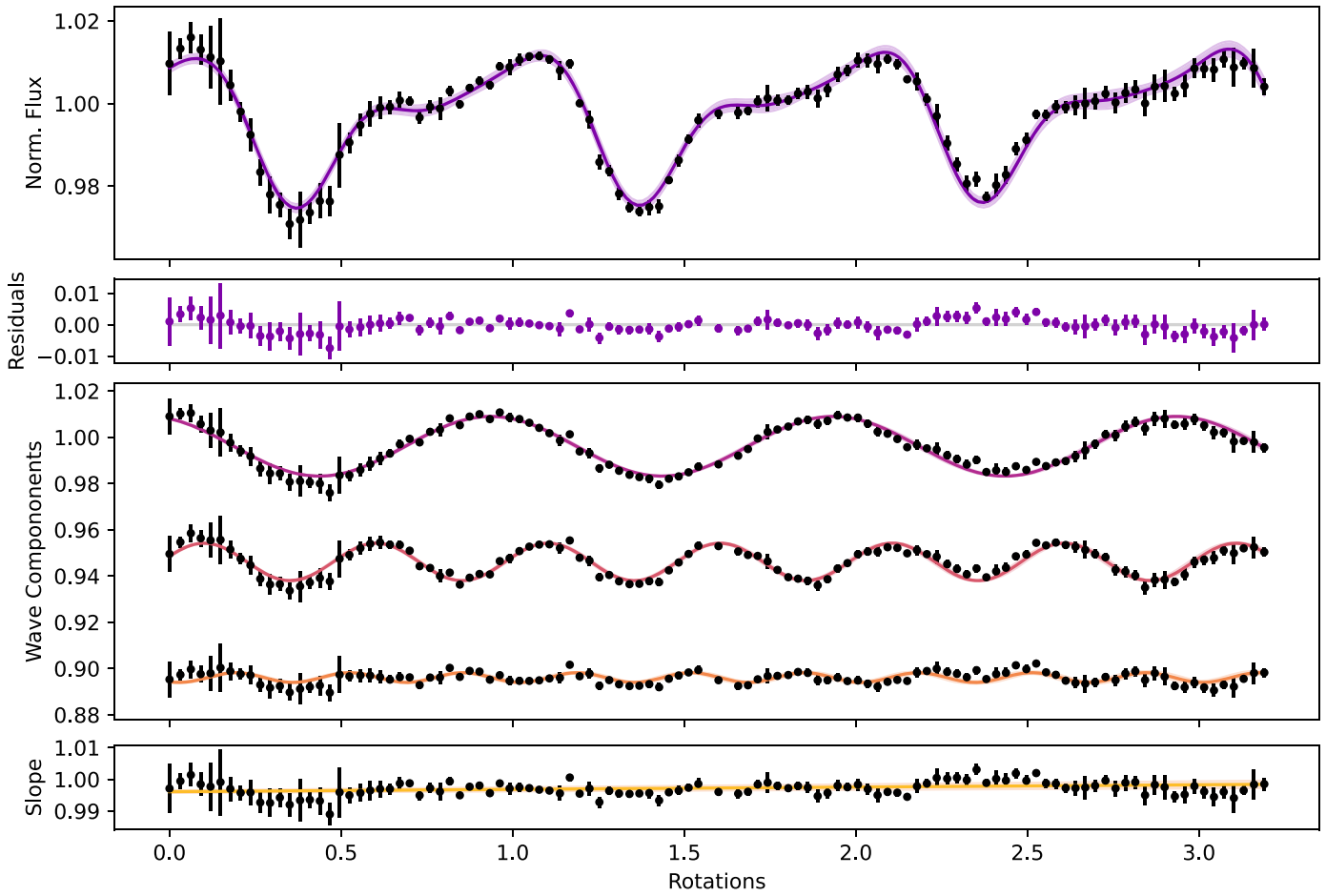

Figure 4. High-cadence 2012 October 14 *J*-band observations and three-wave model. Shaded regions are 1σ uncertainty. Rotations are based on a period of 2.414 hr (Yang et al. 2016). (Top) The inferred three-wave model fitted to observations. (Second row) Residuals. (Third row) Three-wave components with wavenumbers (k) $\approx$ 1, 2, and 3 and periods of 2.41 hr, 1.21 hr, and 0.80 hr, respectively. To demonstrate each component wave's fit, the remaining waves and long-term linear terms are subtracted from the data. (Bottom) Linear term with wave components subtracted from the data.

differential rotation would disperse coherently structured spot groupings.

The retrieved spots' polar latitudes also argue against a spotted model explaining SIMP0136's variability. When exploring different inclinations through GCMs, objects viewed equator-on generate higher-variability light curves than those viewed pole-on (Tan & Showman 2021b). For rotational periods on the scale of SIMP0136 ($\sim$2.5 hr), GCMs also demonstrate that equatorial regions have more enhanced temperature variation and cloud vertical extent than polar latitudes. This is in alignment with observations indicating that brown dwarfs' equatorial regions are more variable and redder (Vos et al. 2017, 2018, 2020, 2022) and also cloudier (Suárez et al. 2023) than higher latitudes. This argument implies that polar structures similar to Saturn's polar hexagonal feature (Godfrey 1988) or Jupiter's circumpolar cyclones (Bolton et al. 2017; Orton et al. 2017; Adriani et al. 2018) are also unlikely to be the dominant driver of SIMP0136's variability.

5.2. Planetary-scale Waves in Substellar Atmospheres

The preference for atmospheric waves found in this work is in agreement with prior studies of SIMP0136 photometry (Apai et al. 2017; McCarthy et al. 2024) as well as other L/T transition dwarfs (e.g., Apai et al. 2021; Zhou et al. 2022; Fuda et al. 2024). Similar to our results in Sections 4.1 and 4.2, peak signals corresponding to $k = 1$ and $k = 2$ waves have been previously identified for SIMP0136 (Apai et al. 2017). Based on observations over hundreds of rotations and thousands of hours, Luhman 16B has been found to also contain signals corresponding to groups of $k = 1, 2$ waves with three to four sine waves accounting for long-term light-curve variability (Apai et al. 2021; Fuda et al. 2024). These results suggest latitudinal variation in wind speeds and atmospheric waves within a banded structure (Fuda et al. 2024). For VHS 1256 b, a three-wave model was found to best fit observations over two rotations (Zhou et al. 2022). The three-wave model was comprised of two waves (P_1, $P_2 = 18.8 \pm 0.2$ hr, 15.1 ± 0.2 hr), less than the rotational period (22.02 ± 0.04 hr; Zhou et al. 2020), forming a beating pattern and a third, $k = 2$ wave with $P_3 = 10.6 \pm 0.1$ hr (Zhou et al. 2022).

Brown dwarf 3D GCMs also support atmospheric waves driving variability at equatorial latitudes. For rapid rotators like SIMP0136, GCMs exhibit equatorial waves with longer zonal wavelengths and lower wavenumber values (similar to those found in Sections 4.1 and 4.2), as well as the enhanced cloud coverage and temperature variation in their equatorial regions discussed in Section 5.1 (Tan & Showman 2021b). Strong evidence is also found for cloud radiative feedback-driven Kelvin waves (and more tentative evidence for Rossby waves) zonally propagating at equatorial latitudes, contributing to

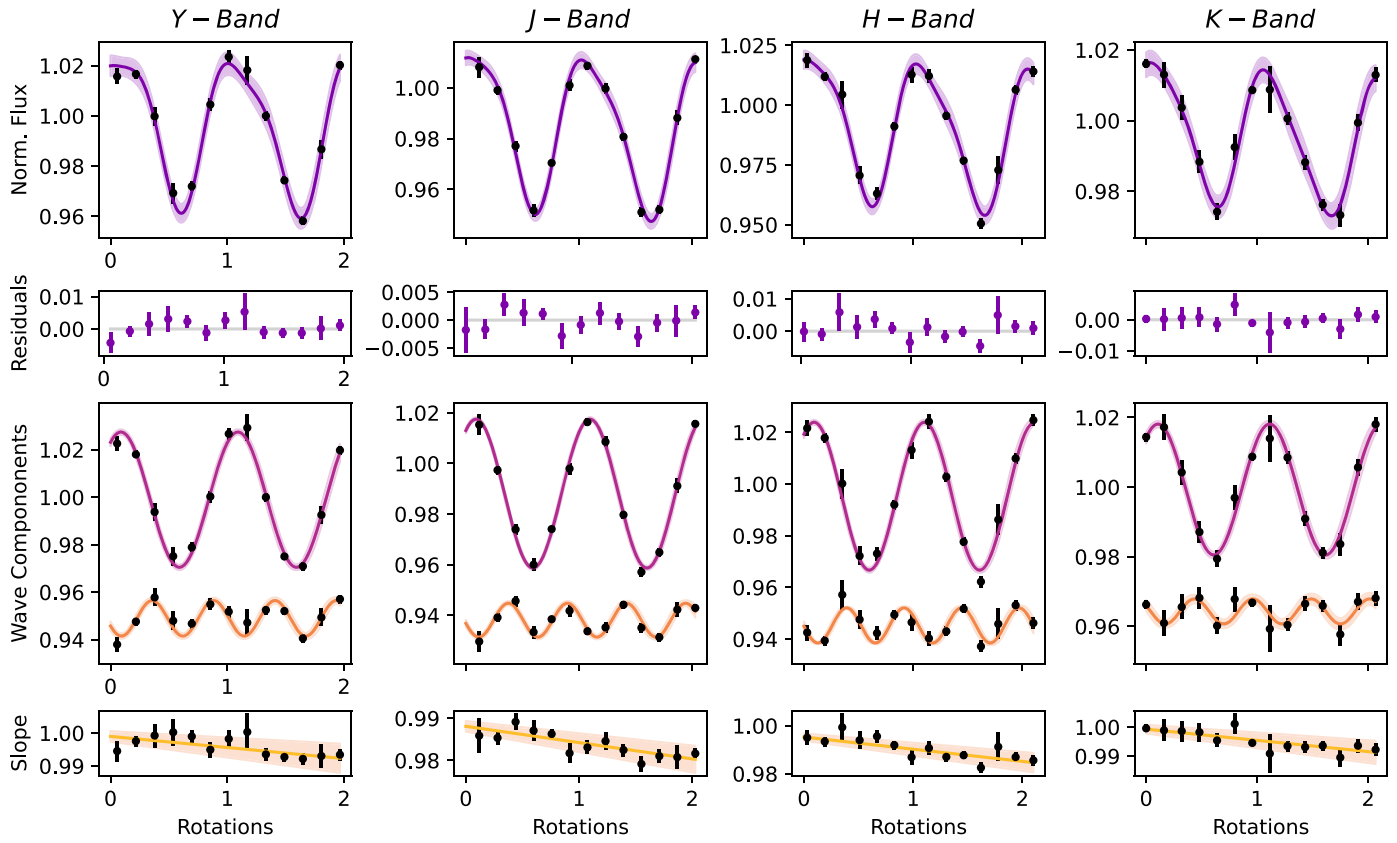

Figure 5. Low-cadence 2012 October 15 $Y/J/H/K$-band observations and two-wave models. Shaded regions are 1σ uncertainty. Rotations are based on a period of 2.414 hr (Yang et al. 2016). (Top row) Inferred two-wave model fitted to observations. (Second row) Residuals. (Third row, first column) Y-band components with wavenumbers (k) $\approx$ 1 and 2 and periods of 2.42 hr and 1.27 hr, respectively. (Third row, second column) J-band components with wavenumbers (k) $\approx$ 1 and 2 and periods of 2.43 hr and 1.26 hr, respectively. (Third row, third column) H-band components with wavenumbers (k) $\approx$ 1 and 2 and periods of 2.44 hr and 1.27 hr, respectively. (Third row, fourth column) K-band components with wavenumbers (k) $\approx$ 1 and 2 and periods of 2.43 hr and 1.27 hr, respectively. (Bottom row) Linear term data and fit. Each wave component and linear term is decomposed as described in Figure 4.

light-curve variability (Tan & Showman 2021b). Kelvin waves move along a barrier, which in this case is formed by the equator (along which the wave moves eastward); essentially, the forces pushing the fluid poleward due to a pressure gradient are balanced by Coriolis forces acting toward the equator in eastward-moving fluids (e.g., Gill 1982). Rossby waves, an additional species of large-scale atmospheric wave, are driven by the conservation of potential vorticity (a fluid mechanics analog to the conservation of angular momentum) and the variation of the Coriolis parameter with latitude (Rossby 1945).

Planetary-scale waves have been observed to play an important role in the atmospheric dynamics of Jupiter. Quasi-stationary and alternating patterns of relatively cloud-free NIR hot spots and cooler ammonia cloud-enhanced plumes have long been observed to be associated with the jet at the boundary of Jupiter's North Equatorial Belt and equatorial zone (Choi et al. 2013). These features are widely considered to be driven by a Rossby wave within Jupiter's equatorial region (Allison 1990; Showman & Dowling 2000; Friedson 2005) with the wave crests correlating to the ammonia aerosol-enhanced plumes and troughs with cloud-free regions due to condensate sublimation (de Pater et al. 2016; Fletcher et al. 2016, 2020).

5.3. Cloud Modulation and Breakup Associated with Atmospheric Waves

Multiband photometry offers the opportunity to explore if cloud modulation associated with planetary-scale waves (as seen in brown dwarf GCMs and observations of Jupiter) exists in SIMP0136's weather layer. If the variability from the waves is associated with silicate and metal clouds (Suárez & Metchev 2022; Vos et al. 2023; McCarthy et al. 2024), the light-curve minima are where we would expect cloud coverage. In this scenario, the light-curve maxima would be associated with hot spots, atmospheric areas of depleted aerosols in which light from deeper atmospheric layers is observable. We expect clouds to scatter and therefore redden light, and indeed, cloudier brown dwarfs have been found to be redder than less cloudy objects (Suárez & Metchev 2022). Light-curve minima should be redder and maxima bluer if this hypothesis is true. A lack of correlation between the light curves and NIR color might support an alternate theory such as convective fingering (Tremblin et al. 2016, 2019).

To date, conclusive color variability has not been detected in SIMP0136 or similar L/T transition objects. Artigau et al. (2009) reported correlated J- and K_S-band light curves ($\frac{\Delta K_S}{\Delta J} = 0.46 \pm 0.06$) for SIMP0136, which they found to best fit a scenario with dusty clouds in a clear atmosphere with two temperature components. Radigan et al. (2012) recorded comparable results ($\frac{\Delta H}{\Delta J}$ and $\frac{\Delta K_S}{\Delta J}$) for 2MASS J21392676 +0220226 (2M2139, T1.5; Reid et al. 2008) and found that the data suggested that these ratios may be variable, particularly $\frac{\Delta K_S}{\Delta J}$. Using HST data, Apai et al. (2013) detected shallow $J-H$ color variability for both SIMP0136 and 2M2139.

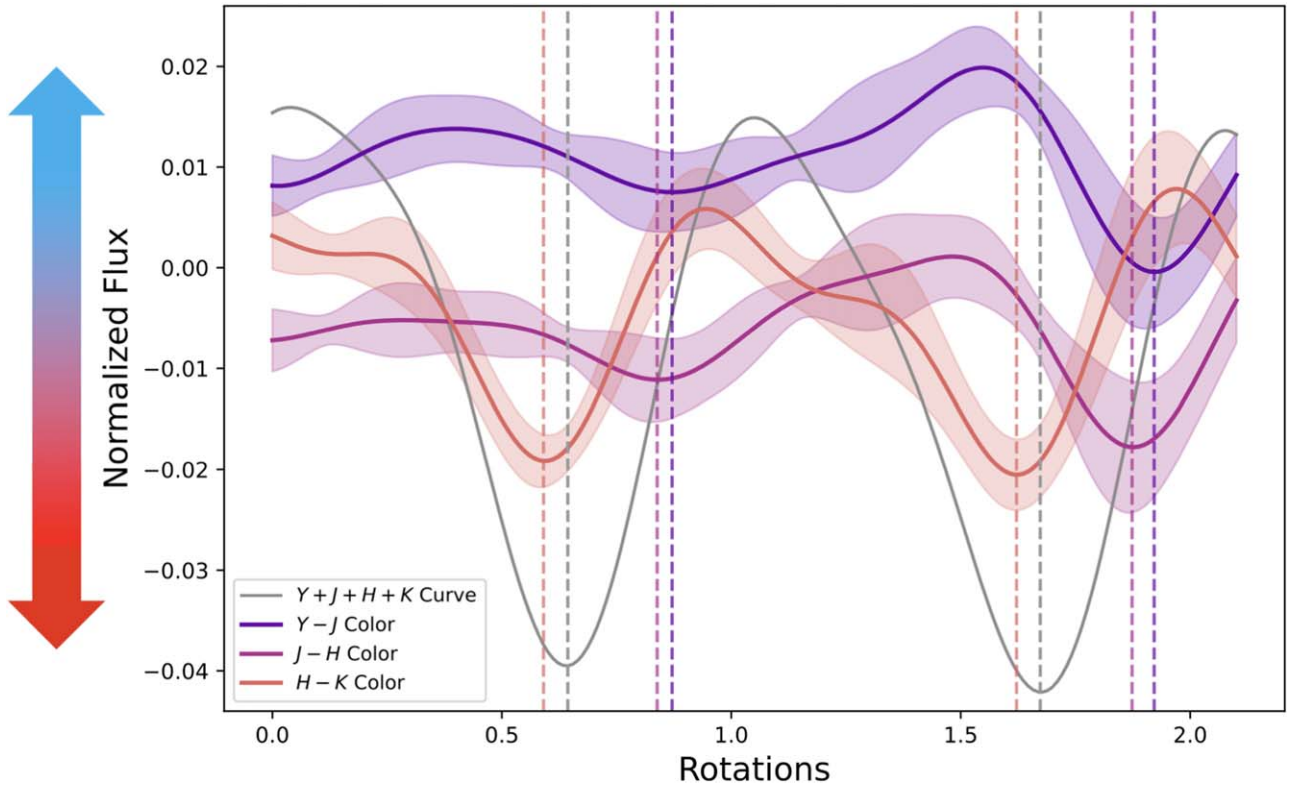

Figure 6. Color time series comparison to composite $Y+J+H+K$ light curve (gray). Shaded regions are 1σ uncertainty. Vertical dashed lines denote color series and light-curve minima. Qualitatively, it can be seen that the composite light-curve minima correspond to reddening (i.e., low flux in $Y-J$, $J-H$, and $H-K$ corresponds to redder color indices). This provides evidence for cloud scattering (see Section 5.3). Light-curve maxima correspond to bluer, presumably relatively cloud-free regions. The $Y-J$ and $J-H$ color series are approximately in phase, but the $H-K$ solution is ∼90° out of phase with the remaining color series, offering evidence of SIMP0136's complex vertical cloud structure.

Lew et al. (2020) found similarly negligible $J-H$ variability across a population of L/T transition substellar objects including SIMP0136. Recently, a $J-K_S=0.03$ color change was reported by McCarthy et al. (2024) using NIR photometry collected with the 1.8 m Perkins Telescope Observatory, perhaps indicating that redder wavelengths should be considered for color variability studies.

Using the $Y/J/H/K$ 2012 October 15 photometry, we conduct a preliminary analysis to determine if the light-curve minima are associated with redder NIR colors and if light-curve maxima are associated with corresponding bluer colors. As a proxy for color, we use the normalized flux of the two-wave models to create $Y-J$, $J-H$, and $H-K$ color time series (see Figure 6). Qualitatively, it can be seen that for each color series, the light curve (here we use the simultaneously inferred composite $Y+J+H+K$ curve) minima approximately correspond to significant dips toward redder colors, while maxima correspond to bluer colors. This behavior is more pronounced for longer wavelengths (e.g., $H-K$). The $H-K$ color time series leads the composite $Y+J+H+K$ curve to a small degree, while $Y-J$ and $J-H$ each lag the light-curve minima. We interpret these results as tentative evidence for complex vertical cloud structures with (presumably silicate and metal) clouds located at the minima and cloud-free regions existing at the maxima due to condensate sublimation.

Follow-up observations using, ideally, space-based platforms with NIR and mid-IR (MIR) spectroscopic capabilities such as the James Webb Space Telescope (JWST) would have the capability to gather broad wavelength time series (see, e.g., JWST Cycle 2 GO Program 3548; PI: J. Vos). With these data, broadband flux variations could be compared to variations in cloud coverage and chemical abundances, further constraining the nature of planetary-scale waves.

5.4. Phase Shifts between NIR Bands

As wavelengths are sensitive to different pressure levels in brown dwarf and planetary atmospheres (e.g., Figure 4 in McCarthy et al. 2024), phase shifts between NIR bands can indicate inhomogeneity in their vertical structures. Space-based observations over baselines ranging between ∼5 and 50 hr detected large phase shifts (∼90°–180°) between shorter NIR bands (e.g., J and K) and longer wavelengths (e.g., Spitzer/Infrared Array Camera Ch. 1 [3.6 μm] and Ch. 2 [4.5 μm]; Buenzli et al. 2012; Yang et al. 2016) for 2MASS J22282889–4310262 (T6.5; Burgasser et al. 2003), 2MASS J15074769–1627386 (L5; Reid et al. 2000), and 2MASS J18212815+1414010 (L5; Looper et al. 2008).

L/T transition objects such as VHS 1256 b, Luhman 16B (T0.5), 2M2139, and SIMP0136 have demonstrated, in general, subtler phase shifts than earlier L and later T dwarfs. Zhou et al. (2022) collected 42 hr of time series observations of VHS 1256 b using the HST/Wide Field Camera 3 (WFC3) and identified no discernible phase shift between the F127M (1.270 ± 0.035 μm), F139M (1.385 ± 0.035 μm), and F153M (1.530 ± 0.035 μm) filters. Observing Luhman 16B with a 2.2 m ground-based telescope over 4 hr in optical and NIR bands, Biller et al. (2013) detected significant phase offsets between K-band light curves and both the H and z' bands. However, observing the same object over 6.5 hr with

HST/WFC3, Buenzli et al. (2015) found the J, H, and water bands to all be in phase. Apai et al. (2013) did not find phase shifts in either 2M2139 or SIMP0136 using HST/WFC3 G141 data over baselines of ∼5.9 hr and ∼3.1 hr, respectively, but Yang et al. (2016) found modest phase shifts (∼30°) between light curves derived from HST/WFC3 G141 and Spitzer Ch. 1 and Ch. 2 over baselines of ∼10 hr. McCarthy et al. (2024) similarly found phase shifts between the J and K_s bands of $39\overset{\circ}{.}9^{+3.6^\circ}_{-1.1^\circ}$ using a 1.8 m ground-based telescope over a 8.5 hr baseline.

Considering the color time series in Figure 6, it can be qualitatively seen that the $H-K$ series is offset by ∼90° from the $J-H$ and $Y-J$ color series, which are approximately in phase with one another. Adopting a similar approach as McCarthy et al. (2024), we use the `signal` function within `Scipy` (Virtanen et al. 2020) to determine the phase shift via cross-correlation. Performing cross-correlation on 5000 samples from the $H-K$ and $J-H$ solutions provides a phase shift of $93\overset{\circ}{.}8 \pm 7\overset{\circ}{.}4$. This 12.7σ detection provides evidence for complex vertical cloud structure between the pressure levels corresponding to these NIR bands, likely in the form of multiple cloud layers as suggested by Vos et al. (2023) and McCarthy et al. (2024).

Statistically significant phase shifts between the inferred NIR-band wave components are not detected for SIMP0136 in this work (see Table 3). Within each band, the $k=1$ and $k=2$ components are offset by approximately 100°–140° from one another. The $k=1$ components each have phases ranging from ∼52° to 58°. The $k=2$ components have phases ranging from ∼150° to 205°. For both $k=1$ and $k=2$ waves, the phase shifts between NIR bands are less than the 3σ uncertainty.

Higher-cadence observations in both the NIR and MIR, such as those possible with the JWST, would be able to reduce phase uncertainty and detect phase shifts at lower pressure levels (higher altitudes). Such detections would provide further collaborating evidence of cloud modulation associated with planetary-scale waves along with a more complete picture of SIMP0136's vertical architecture.

6. Summary

To determine the driving source of spectrophotometric variability in SIMP0136, an L/T transition object, we analyze NIR photometry collected at the CFHT on the nights of 2012 October 14 and 2012 October 15. The data provide coverage for ≳five rotations of SIMP0136. We modify the publicly available open-source Python code `Imber` (Plummer 2023, 2024a), developed and honed in Plummer & Wang (2022, 2023), to fit the observed light curves with waves as well as spotted models. Here are our findings.

1. The 2012 October 14 high-cadence J-band observations are best fit with a three-wave model consisting of $k=1$, 2, and 3 components with periods of 2.41 hr, 1.21 hr, and 0.80 hr (see Section 4.1). A linear term with a positive slope is also retrieved and indicates an increase in flux throughout the observation.
2. The October 15 low-cadence $Y/J/H/K$ light curves are each fit with two-wave models with $k=1$ and 2 components (see Section 4.2). Each of these components has periods approximating the rotational period and half the rotational period. In each of the inferred models, the linear term has a negative slope, demonstrating a change from the prior night's observations.
3. For the spotted models, the retrieved spot radii exceed the Rossby deformation radius (and Rhines scale for the dark spot) at the inferred latitudes and assumed mean flow speed and planetary radius, indicating that such spots are likely to be unphysical (see Section 5.1).
4. For the multiband ($Y/J/H/K$) photometry, the inferred two-wave models demonstrate a correlation with shifts in color (see Section 5.3). The light-curve minima appear to correspond to redder colors, while the maxima correspond to bluer flux. This correlation is strongest for the $H-K$ color time series. We propose that this may be tentative evidence for planetary-scale waves traveling in the vertical plane of SIMP0136's atmosphere with enhanced silicate or iron cloud coverage in the wave crests and depleted aerosols in the troughs.
5. We detect a $93\overset{\circ}{.}8 \pm 7\overset{\circ}{.}4$ (12.7σ) phase offset between the $H-K$ and $J-H$ color series, providing evidence for complex vertical cloud structure in SIMP0136's atmosphere (see Section 5.4).

Moving forward, a greater understanding of the true nature of planetary-scale waves potentially driving brown dwarf and planetary-mass object variability can be achieved by multi-rotational and quasi-simultaneous observations in the NIR and MIR by platforms such as JWST. Spectroscopic modes would help to discern if the reddening associated with NIR light-curve minima is tied to variations in cloud coverage or chemical abundances. Both photometric and spectroscopic modes could further constrain phase shifts between the NIR and MIR bands and color indices, providing a greater understanding of SIMP0136's vertical structure throughout its atmospheric layers.

Acknowledgments

M.K.P. would like to thank the United States Air Force Academy's Department of Physics and Meteorology, the United States Air Force Institute of Technology's Civilian Institution Program, and The Ohio State University's Department of Astronomy for supporting and enabling this research. J.W. acknowledges the support by the National Science Foundation under grant No. 2143400. Additionally, we want to acknowledge the hard work and expertise of the scientific, technical, and administrative staff at the Canada–France–Hawaii Telescope. We thank Leigh N. Fletcher for his professional insight on solar system atmospheres. We thank the anonymous reviewer for the constructive feedback and comments. We would also like to thank the Group for Studies of Exoplanets (GFORSE) at The Ohio State University, Department of Astronomy, for continuous feedback throughout the development of this research.

The results presented in this paper are based on observations obtained at the Canada–France–Hawaii Telescope (CFHT), which is operated by the National Research Council (NRC) of Canada, the Institut National des Sciences de l'Univers of the Centre National de la Recherche Scientifique (CNRS) of France, and the University of Hawaii. Based on observations obtained with WIRCam, a joint project of CFHT, Taiwan, Korea, Canada, and France at the CFHT. The observations at the CFHT were performed with care and respect from the

summit of Maunakea, which is a significant cultural and historic site.

This paper includes data collected by the TESS mission. Funding for the TESS mission is provided by NASA's Science Mission Directorate.

The views expressed in this article are those of the author and do not necessarily reflect the official policy or position of the Air Force, the Department of Defense, or the U.S. Government.

Software: Imber (Plummer 2023, 2024a), Astropy (Astropy Collaboration et al. 2013, 2018, 2022), Dynesty (Speagle 2020), Lightkurve (Lightkurve Collaboration et al. 2018), Matplotlib (Hunter 2007), Pandas (McKinney et al. 2010), Scipy (Virtanen et al. 2020).

Appendix
Reference Stars

In our analysis above, we assumed that the reference stars are sufficiently stable on timescales commensurate with the rotation period of SIMP0136 to serve as photometric calibrators. Reference stars were chosen based on their location on the same WIRCam science array as SIMP0136, their brightness ($J < 12.8$), and the need for these stars' signals to be unsaturated and unaffected by known bad pixels. Coordinates and *JHK* magnitudes of the reference stars used in our photometric analysis are listed in Table 1. Four stars have closely matching colors ($J - K$ ranging from 0.367 to 0.396), while star #1 has a significantly redder $J - H = 0.89$.

While there is no simultaneous external calibration of the photometric stability of our reference stars, TESS provides month-long observations of nearly the entire sky. The SIMP0136 field has been visited once by TESS (Sector 42, 2021 August–September), providing time series of our reference stars. SIMP0136 is too faint for useful monitoring with TESS due to its extremely red optical-to-infrared colors, but the five reference stars are sufficiently bright for useful photometry to be retrieved. We extracted their background-subtracted light curves with the LIGHTKURVE package (Lightkurve Collaboration et al. 2018). These observations provide insight into the variability of our reference stars. As shown in Figure 7, none of the stars display short-timescale percent-level variability, and they do not display significant periodicity above the 1% FAP level for periods shorter than 1 day.

We investigated possible correlations between observing conditions and reference star fluxes. Figures 8 and 9 illustrate the fluxes measured as a function of seeing and air mass, respectively. There is an anticorrelation of flux with both quantities in both day 1 (*J*-only) and day 2 (interleaved *YJHK*) data sets.

The purpose of reference stars is to account, at least to first order, for these extinction effects; we therefore showed each reference star dependency against seeing and air mass once corrected by the sum of all other reference stars (right panels of Figures 8 and 9). No trend is seen after correction by reference stars at this step, and we conclude that reference stars are, for all practical purposes, stable to well within 1%.

The dependency of raw fluxes against air mass can easily be understood as an increase in atmospheric extinction at higher air mass, while the dependency with seeing probably arises from a combination of aperture losses as well as the covariance of seeing with air mass (i.e., a worsening seeing correlates with higher extinction as both happen at a higher air mass). Figure 10 shows the changes of seeing, median sky level, and air mass through our data sets. The expected mild correlation of seeing and sky background is seen mostly on day 1. Day 2 observations are shorter and explore a smaller air-mass range.

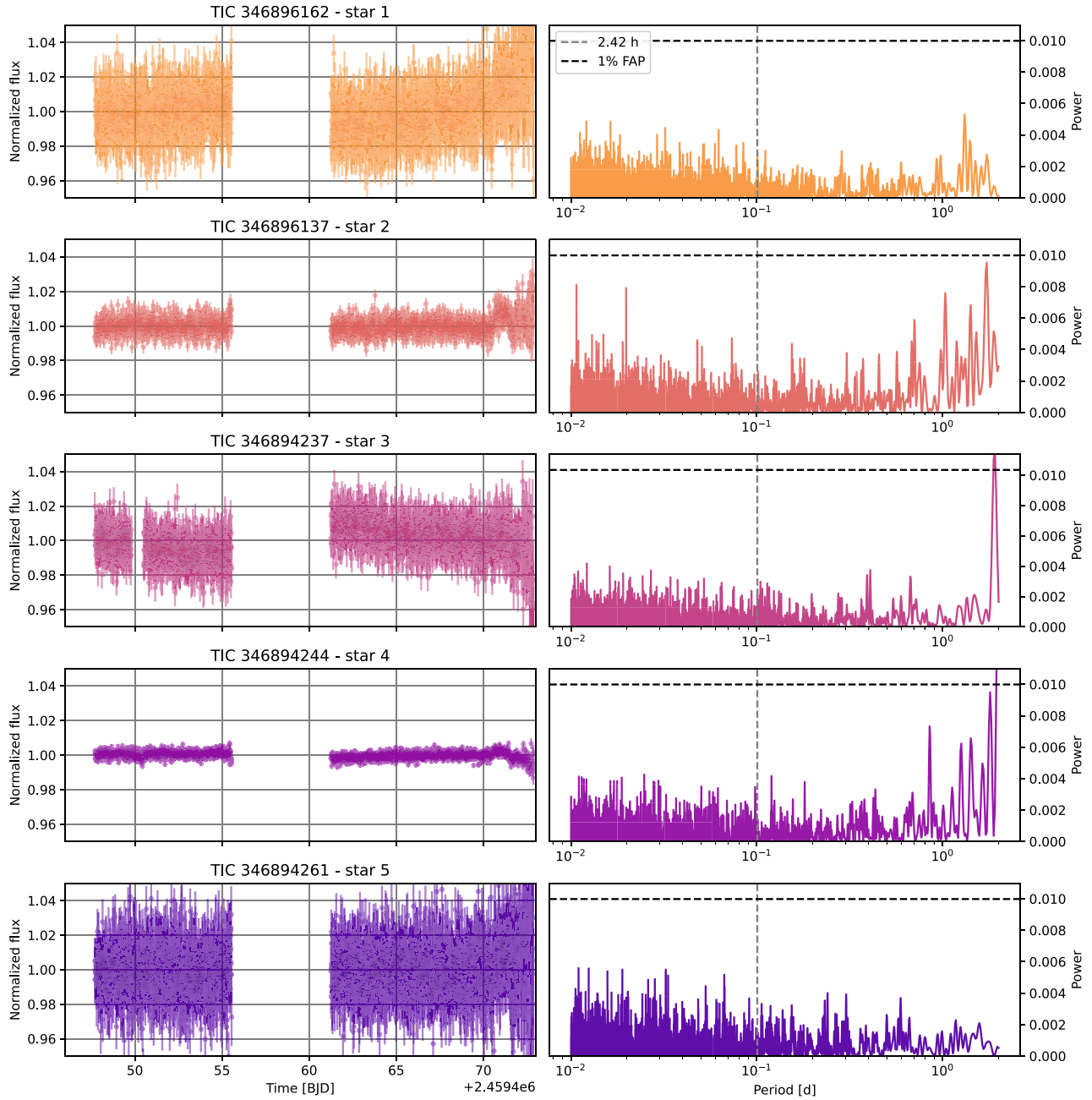

Figure 7. TESS photometric light curves for the five reference stars (left). None of the stars display short-term (<1 day) variability above a 1% FAP, and no signal is seen close to the rotation period of SIMP0136.

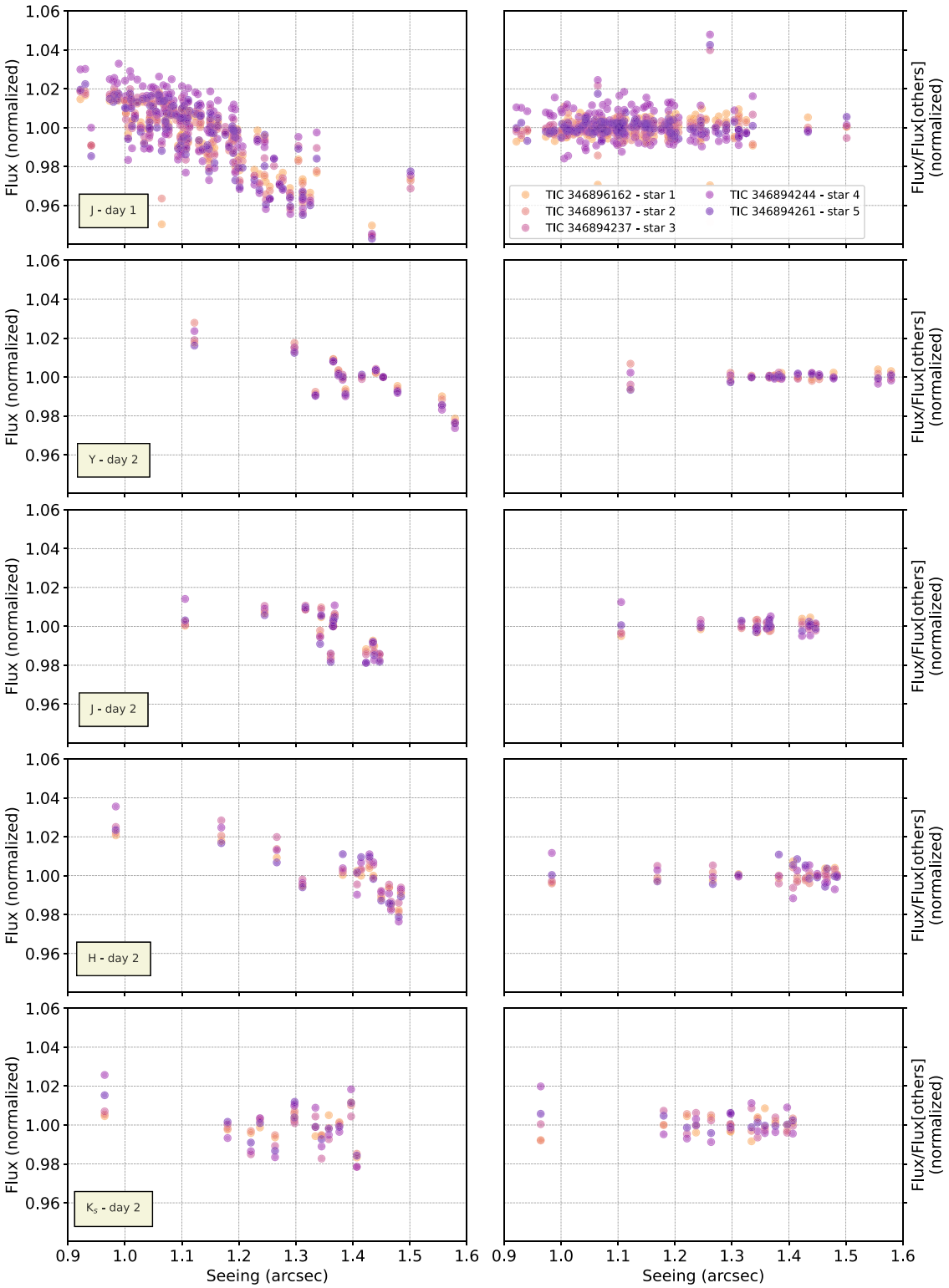

Figure 8. Correlation of normalized raw fluxes of reference stars against seeing (left). Each reference star flux has been normalized to its median; one sees a ∼6% loss in flux between measurements with a seeing of $\sim 0\farcs9$ and $\sim 1\farcs6$. To assess if differential biases were present in our photometric measurements, we compared each of the reference stars to the average of all stars (right) against seeing. The calibrated fluxes show no dependency against seeing, which confirms that our reference stars will serve their purpose in calibrating SIMP0136 time series.

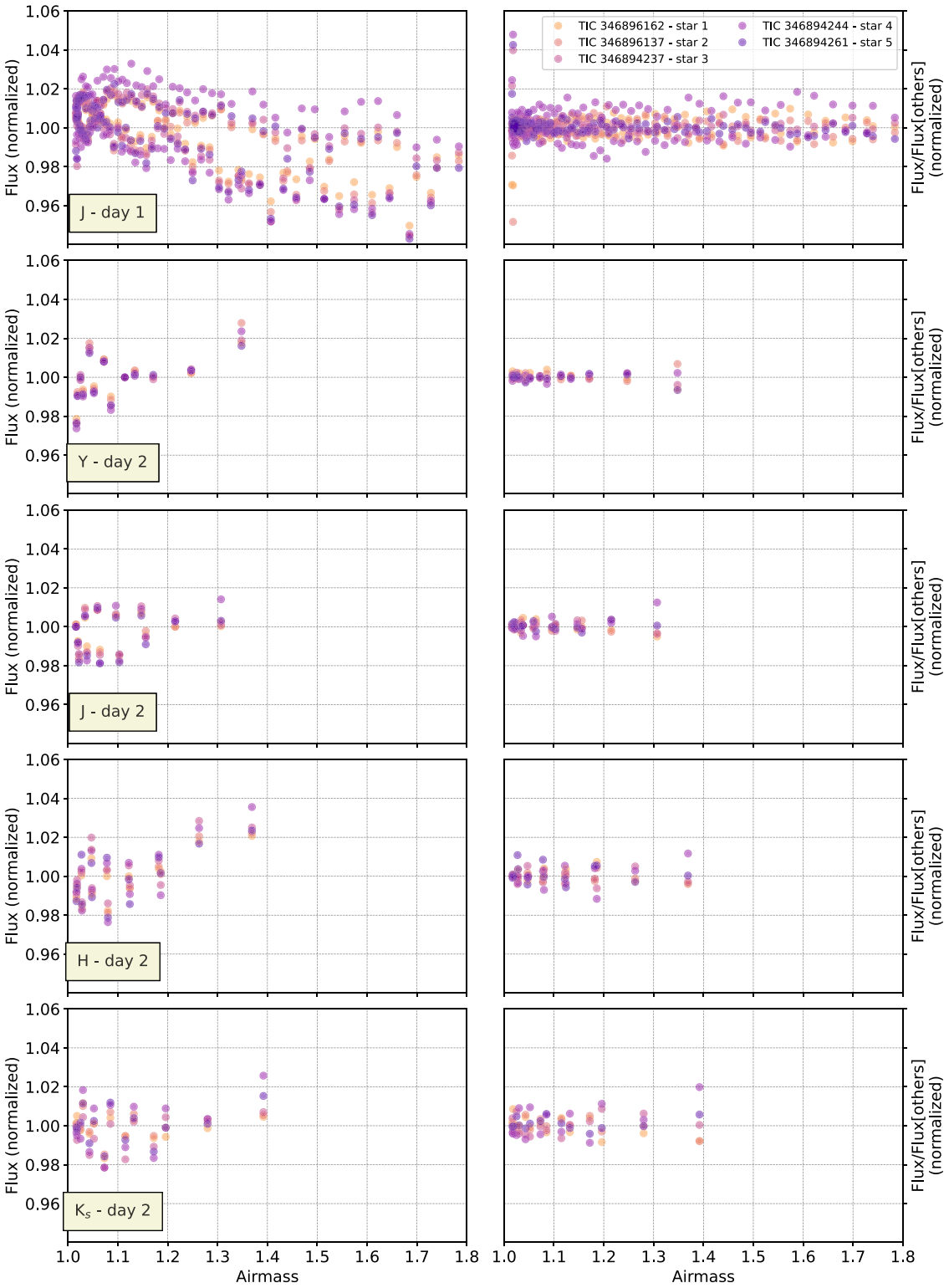

Figure 9. Same as Figure 8 but for the dependency of fluxes (raw and corrected) with air mass.

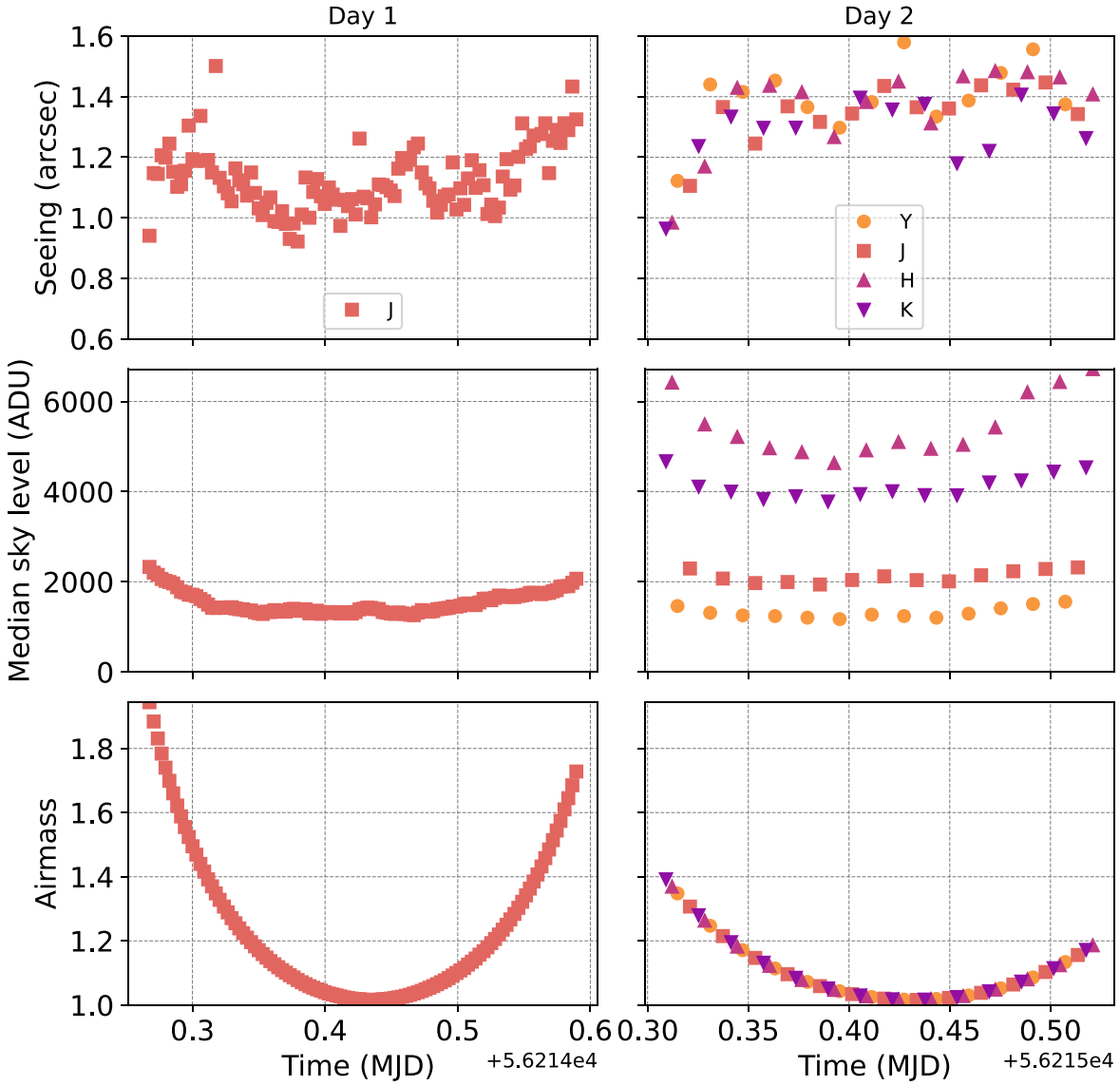

Figure 10. Variation of the seeing, median sky background, and air mass through the *J*-band observing night. Sky background and, to a lesser extent, seeing are correlated with the air mass through the observing sequence.

ORCID iDs

Michael K. Plummer https://orcid.org/0000-0002-4831-0329
Ji Wang (王吉) https://orcid.org/0000-0002-4361-8885
Étienne Artigau https://orcid.org/0000-0003-3506-5667
René Doyon https://orcid.org/0000-0001-5485-4675
Genaro Suárez https://orcid.org/0000-0002-2011-4924

References

Ackerman, A. S., & Marley, M. S. 2001, ApJ, 556, 872
Adriani, A., Mura, A., Orton, G., et al. 2018, Natur, 555, 216
Allers, K. N., Vos, J. M., Biller, B. A., & Williams, P. K. G. 2020, Sci, 368, 169
Allison, M. 1990, Icar, 83, 282
Apai, D., Karalidi, T., Marley, M. S., et al. 2017, Sci, 357, 683
Apai, D., Nardiello, D., & Bedin, L. R. 2021, ApJ, 906, 64
Apai, D., Radigan, J., Buenzli, E., et al. 2013, ApJ, 768, 121
Artigau, É., Bouchard, S., Doyon, R., & Lafrenière, D. 2009, ApJ, 701, 1534
Artigau, É., Doyon, R., Lafrenière, D., et al. 2006, ApJL, 651, L57
Astropy Collaboration, Price-Whelan, A. M., Lim, P. L., et al. 2022, ApJ, 935, 167
Astropy Collaboration, Price-Whelan, A. M., Sipőcz, B. M., et al. 2018, AJ, 156, 123
Astropy Collaboration, Robitaille, T. P., Tollerud, E. J., et al. 2013, A&A, 558, A33
Biller, B. A., Crossfield, I. J. M., Mancini, L., et al. 2013, ApJL, 778, L10
Bolton, S. J., Adriani, A., Adumitroaie, V., et al. 2017, Sci, 356, 821
Buenzli, E., Apai, D., Morley, C. V., et al. 2012, ApJL, 760, L31
Buenzli, E., Saumon, D., Marley, M. S., et al. 2015, ApJ, 798, 127
Burgasser, A. J., Kirkpatrick, J. D., Brown, M. E., et al. 1999, ApJL, 522, L65
Burgasser, A. J., Marley, M. S., Ackerman, A. S., et al. 2002, ApJL, 571, L151
Burgasser, A. J., McElwain, M. W., & Kirkpatrick, J. D. 2003, AJ, 126, 2487
Burrows, A., Hubbard, W. B., Lunine, J. I., & Liebert, J. 2001, RvMP, 73, 719
Burrows, A., & Sharp, C. M. 1999, ApJ, 512, 843
Burrows, A., Sudarsky, D., & Hubeny, I. 2006, ApJ, 640, 1063
Cho, J. Y. K., & Polvani, L. M. 1996, Sci, 273, 335
Choi, D. S., Showman, A. P., Vasavada, A. R., & Simon-Miller, A. A. 2013, Icar, 223, 832
Croll, B., Muirhead, P. S., Lichtman, J., et al. 2013, arXiv:1609.03587
Crossfield, I. J. M., Biller, B., Schlieder, J. E., et al. 2014, Natur, 505, 654
Cushing, M. C., & Roellig, T. L. 2006, in ASP Conf. Ser. 357, The Spitzer Space Telescope: New Views of the Cosmos, ed. L. Armus & W. T. Reach (San Francisco, CA: ASP), 66
Cutri, R. M., Skrutskie, M. F., van Dyk, S., et al. 2003, yCat, II/246
de Pater, I., Sault, R. J., Butler, B., DeBoer, D., & Wong, M. H. 2016, Sci, 352, 1198

Eriksson, S. C., Janson, M., & Calissendorff, P. 2019, A&A, 629, A145
Fletcher, L. N., Greathouse, T. K., Orton, G. S., et al. 2016, Icar, 278, 128
Fletcher, L. N., Orton, G. S., Greathouse, T. K., et al. 2020, JGRE, 125, e06399
Friedson, A. J. 2005, Icar, 177, 1
Fuda, N., Apai, D., Nardiello, D., et al. 2024, ApJ, 965, 182
Gagné, J., Faherty, J. K., Burgasser, A. J., et al. 2017, ApJL, 841, L1
Gaia Collaboration, Vallenari, A., Brown, A. G. A., et al. 2023, A&A, 674, A1
Gauza, B., Béjar, V. J. S., Pérez-Garrido, A., et al. 2015, ApJ, 804, 96
Gill, A. E. 1982, Atmosphere-Ocean Dynamics (Orlando: Academic Press)
Godfrey, D. A. 1988, Icar, 76, 335
Gray, D. F. 2008, The Observation and Analysis of Stellar Photospheres (Cambridge: Cambridge Univ. Press)
Haqq-Misra, J., Wolf, E. T., Joshi, M., Zhang, X., & Kopparapu, R. K. 2018, ApJ, 852, 67
Higson, E., Handley, W., Hobson, M., & Lasenby, A. 2019, Stat. Comput., 29, 891
Hunter, J. D. 2007, CSE, 9, 90
Karalidi, T., Apai, D., Marley, M. S., & Buenzli, E. 2016, ApJ, 825, 90
Kass, R. E., & Raftery, A. E. 1995, J. Am. Stat. Assoc., 90, 773
Kirkpatrick, J. D. 2005, ARA&A, 43, 195
Knapp, G. R., Leggett, S. K., Fan, X., et al. 2004, AJ, 127, 3553
Lew, B. W. P., Apai, D., Zhou, Y., et al. 2020, AJ, 159, 125
Lightkurve Collaboration, Cardoso, J. V. d. M., Hedges, C., et al. 2018, Lightkurve: Kepler and TESS Time Series Analysis in Python, Astrophysics Source Code Library, ascl:1812.013
Liu, P., Biller, B. A., Vos, J. M., et al. 2024, MNRAS, 527, 6624
Lomb, N. R. 1976, Ap&SS, 39, 447
Looper, D. L., Kirkpatrick, J. D., Cutri, R. M., et al. 2008, ApJ, 686, 528
Luger, R., Bedell, M., Foreman-Mackey, D., et al. 2021, arXiv:2110.06271
Luhman, K. L. 2013, ApJL, 767, L1
McCarthy, A. M., Muirhead, P. S., Tamburo, P., et al. 2024, ApJ, 965, 83
McKinney, W. 2010, in Proc. 9th Python in Science Conf. (Austin, TX: SciPy), 51
Metchev, S., Apai, D., Radigan, J., et al. 2013, AN, 334, 40
Millar-Blanchaer, M. A., Girard, J. H., Karalidi, T., et al. 2020, ApJ, 894, 42
Orton, G. S., Hansen, C., Caplinger, M., et al. 2017, GeoRL, 44, 4599
Plummer, M. 2024a, Imber 3.0: Modeling Spectrophotometric Variability of a Planetary-Mass Object, v3.0, Zenodo, doi:10.5281/zenodo.10729262
Plummer, M. K. 2023, Imber: Doppler Imaging Tool for Modeling Stellar and Substellar Surfaces, Astrophysics Source Code Library, ascl:2307.033
Plummer, M. K. 2024b, mkplummer/Imber: Imber 3.0: Modeling Spectrophotometric Variability of a Planetary-Mass Object, v.3.0, Zenodo, doi:10.5281/ZENODO.10729262
Plummer, M. K., & Wang, J. 2022, ApJ, 933, 163
Plummer, M. K., & Wang, J. 2023, ApJ, 951, 101
Puget, P., Stadler, E., Doyon, R., et al. 2004, Proc. SPIE, 5492, 978
Radigan, J. 2014, ApJ, 797, 120
Radigan, J., Jayawardhana, R., Lafrenière, D., et al. 2012, ApJ, 750, 105
Radigan, J., Lafrenière, D., Jayawardhana, R., & Artigau, E. 2014, ApJ, 793, 75
Reid, I. N., Cruz, K. L., Kirkpatrick, J. D., et al. 2008, AJ, 136, 1290
Reid, I. N., Kirkpatrick, J. D., Gizis, J. E., et al. 2000, AJ, 119, 369
Reiners, A., & Basri, G. 2008, ApJ, 684, 1390
Rhines, P. B. 1975, JFM, 69, 417
Ricker, G. R., Winn, J. N., Vanderspek, R., et al. 2015, JATIS, 1, 014003
Rossby, C. G. 1945, JAtS, 2, 187
Scargle, J. D. 1982, ApJ, 263, 835
Showman, A. P., Cho, J. Y. K., & Menou, K. 2010, in Exoplanets, ed. S. Seager (Tucson, AZ: Univ. of Arizona Press), 471
Showman, A. P., & Dowling, T. E. 2000, Sci, 289, 1737
Showman, A. P., Fortney, J. J., Lewis, N. K., & Shabram, M. 2013, ApJ, 762, 24
Showman, A. P., & Kaspi, Y. 2013, ApJ, 776, 85
Showman, A. P., Tan, X., & Zhang, X. 2019, ApJ, 883, 4
Shuster, M. D. 1993, ITAES, 29, 263
Skilling, J. 2004, in AIP Conf. Ser. 735, Bayesian Inference and Maximum Entropy Methods in Science and Engineering: 24th Int. Workshop on Bayesian Inference and Maximum Entropy Methods in Science and Engineering, ed. R. Fischer, R. Preuss, & U. V. Toussaint (Melville, NY: AIP), 395
Skilling, J. 2006, BayAn, 1, 833
Speagle, J. S. 2020, MNRAS, 493, 3132
Stassun, K. G., Oelkers, R. J., Pepper, J., et al. 2018, AJ, 156, 102
Suárez, G., & Metchev, S. 2022, MNRAS, 513, 5701
Suárez, G., Vos, J. M., Metchev, S., Faherty, J. K., & Cruz, K. 2023, ApJL, 954, L6
Tan, X. 2022, MNRAS, 511, 4861
Tan, X., & Showman, A. P. 2021a, MNRAS, 502, 678
Tan, X., & Showman, A. P. 2021b, MNRAS, 502, 2198
Thanjavur, K., Teeple, D., Yan, C.-H., et al. 2011, in Telescopes from Afar Conf., ed. S. Gajadhar et al., 72
Tremblin, P., Amundsen, D. S., Chabrier, G., et al. 2016, ApJL, 817, L19
Tremblin, P., Padioleau, T., Phillips, M. W., et al. 2019, ApJ, 876, 144
Tsuji, T., & Nakajima, T. 2003, ApJL, 585, L151
Tsuji, T., Ohnaka, K., Aoki, W., & Nakajima, T. 1996, A&A, 308, L29
Virtanen, P., Gommers, R., Oliphant, T. E., et al. 2020, NatMe, 17, 261
Vogt, S. S., Penrod, G. D., & Hatzes, A. P. 1987, ApJ, 321, 496
Vos, J. M., Allers, K. N., & Biller, B. A. 2017, ApJ, 842, 78
Vos, J. M., Allers, K. N., Biller, B. A., et al. 2018, MNRAS, 474, 1041
Vos, J. M., Biller, B. A., Allers, K. N., et al. 2020, AJ, 160, 38
Vos, J. M., Burningham, B., Faherty, J. K., et al. 2023, ApJ, 944, 138
Vos, J. M., Faherty, J. K., Gagné, J., et al. 2022, ApJ, 924, 68
Wilson, P. A., Rajan, A., & Patience, J. 2014, A&A, 566, A111
Yang, H., Apai, D., Marley, M. S., et al. 2016, ApJ, 826, 8
Zhang, X., & Showman, A. P. 2014, ApJL, 788, L6
Zhou, Y., Bowler, B. P., Apai, D., et al. 2022, AJ, 164, 239
Zhou, Y., Bowler, B. P., Morley, C. V., et al. 2020, AJ, 160, 77